Grazing Incidence X-ray Diffraction on Langmuir Films: Toward Atomic Resolution†

J. Pignat,‡,§ J. Daillant,*,‡ L. Leiserowitz,‖ and F. Perrot§

Service de Chimie Moléculaire/LIONS, CEA-Saclay, Bât. 125, F-91191 Gif-sur-Yvette Cedex, France, LPPI, Université de Cergy-Pontoise, 5 mail Gay-Lussac Neuville/Oise, 95031 Cergy-Pontoise Cedex, France, and Department of Materials and Interfaces, The Weizmann Institute of Science, Rehovot 76100, Israel

Received: November 22, 2005; In Final Form: February 16, 2006

We have analyzed grazing incidence diffration (GIXD) data from condensed phases of Langmuir films of long-chain fatty acids at the air−water interface by using a new method consisting of a careful extraction of the structure factors followed by fitting of molecular parameters. We show that, contrary to the general belief, the information contained in GIXD spectra is enough to obtain near-atomic structural information. In particular, we directly determine for the first time the orientation of the chain backbone planes and of the carboxylic headgroups and we evaluate chain conformation defects. This new method allowed us to evidence a new phase of symmetry *p*2*gm* at high pressure, corresponding to a minimum in lattice energy, but never observed.

1. Introduction

Langmuir films of long-chain amphiphiles at the air−water interface present different phases depending on temperature and surface pressure (the difference between the surface tension of pure water and the actual surface tension in the presence of the film $\Pi = \gamma_{H_2O} - \gamma$). Their phase transitions were first identified by isotherm measurements (surface pressure as a function of molecular area for a fixed temperature), and miscibility studies established the correspondence between the phases of different compounds.[1] The first grazing incidence X-ray diffraction (GIXD) experiments directly carried out on monolayers at the air−water interface were reported in 1987,[2,3,4] followed by comprehensive studies of the phase diagrams of fatty acids.[5,6,7] GIXD has now become the primary technique used to determine the structure of amphiphilic monolayers on water (see, for example, refs 8−10 for reviews), allowing the determination of unit cell parameters, molecular tilt angle, and azimuth of tilt direction, which made it possible to demonstrate the close correspondence between the phases of Langmuir films at the air−water interface and bulk smectic or hexatic categories.[1] More recently, GIXD has also been used to study more complex systems of biological interest like cholesterol[11] or peptides forming β-sheets.[12]

As it is, however, generally considered that by going further, the unit cell characterization discussed above is impossible by using purely crystallographic information, the strategy used by a few groups has been to use additional information. A first possibility is to use known information on local packing of long methyl chains in three-dimensional crystals[13] to infer the packing in the two-dimensional mesophases. For example,[10] when represented in the "transverse" plane normal to the molecular axis, all known structures fall with some scatter between rather dense packings with projected areas per chain 0.186 nm^2 (herringbone, HB) and 0.19 nm^2 (pseudo-herringbone,[13] PHB), corresponding to rectangular cells of dimension 0.5×0.75 nm^2 (HB) and 0.44×0.88 nm^2 (PHB). In the HB cell,[14] the angle between the backbone plane of the central molecule in the unit cell and the molecules at the corners is 90°, whereas in the PHB cell this angle is 40°, as confirmed by lattice energy calculations.[15]

Another, more general, strategy for a more complete structural determination than directly available from the diffraction measurements was proposed in ref 16. It consists of constructing a variety of model arrangements (including space group and packing), which may be tested against Bragg-rod data and lattice energy calculations (see also ref 9). Some of the possible plane groups can be ruled out by comparison with the Bragg-rod profiles and others by lattice energy calculations, leading to only a few or, at best, only one possibility. This method was successfully applied to triacontanoic acid,[16] alcohols,[17,18] and fluorocarbons.[19]

In this paper, we use a different method, and we demonstrate that, contrary to the general belief, the information contained in GIXD spectra is enough to directly obtain near-atomic structural information when properly analyzed. Our method consists of a careful extraction of the structure factors from the diffraction data, followed by fitting of molecular parameters such as the orientation of the chain backbone planes, carboxylic headgroup orientation, and chain conformation defects. All of these parameters have a marked influence on the calculated structure factors and can be determined by model fitting. By using this method, we analyzed GIXD spectra from palmitic acid (C_{16}), stearic acid (C_{18}), arachidic acid (C_{20}), and behenic acid (C_{22}) films for different phases during compression. We show that the expected molecular organization inferred from comparison to three-dimensional structure or energy calculations can be directly determined. We also evidence a high-surface-pressure molecular organization (*p*2*gm* symmetry) predicted by lattice energy calculations but never observed before.

The paper is organized as follows. In Section 2, we review the theoretical bases of GIXD; we then give the experimental details (Section 3) and present our method (Section 4). In Section

† Part of the special issue "Charles M. Knobler Festschrift".

* Corresponding author. Jean.Daillant@cea.fr.
‡ Service de Chimie Moléculaire/LIONS, CEA-Saclay.
§ LPPI, Université de Cergy-Pontoise.
‖ Department of Materials and Interfaces, The Weizmann Institute of Science.

10.1021/jp056770k CCC: $33.50 © 2006 American Chemical Society
Published on Web 04/12/2006

5, we demonstrate the sensitivity of the method to the molecular parameters and present the results, which are discussed in Section 6.

2. Grazing Incidence X-ray Diffraction

Crystals are defined by the periodic repetition of an atomic pattern in space. For a three-dimensional crystal, this periodicity is described by the three vectors **a**, **b**, and **c** defining the unit cell, whereas only two vectors **a** and **b** are enough to describe the two-dimensional films considered in this paper. As the elastic (Thomson) scattering of X-rays is due to electrons, an important quantity is the unit cell electron density $\rho(\mathbf{r})$. The waves scattered by two electrons distant from **r** differ by a phase factor $\exp(i\mathbf{q}\cdot\mathbf{r})$, where the wave-vector transfer **q** is the difference between the wave-vectors $\mathbf{k}_{in}$ in the incident direction and $\mathbf{k}_{sc}$ in the scattering direction, both of magnitude $k_0 = 2\pi/\lambda$, with λ the wavelength. Within the Born approximation (kinematic approximation), the amplitude of the scattered wave is simply proportional to the Fourier transform of the electron density. The scattered intensity can be written:

$$I \propto |F(\mathbf{q})|^2 \times |S(\mathbf{q})|^2$$

with $F(\mathbf{q}) = \int \rho(\mathbf{r}) \exp(i\mathbf{q}\cdot\mathbf{r})\, d\mathbf{r}$ the structure factor describing the unit cell atomic composition and structure, and $S(\mathbf{q})$ the lattice summation factor describing the repetition in space:

$$S(\mathbf{q}) = \sum_{i_1=1}^{N_1} \sum_{i_2=1}^{N_2} e^{i(\mathbf{q}\cdot\mathbf{a})i_1 + i(\mathbf{q}\cdot\mathbf{b})i_2} \quad (1)$$

with N_1 and N_2 the number of repeat units along **a** and **b** respectively.

As the refractive index of X-rays is slightly smaller than 1, $n = 1 - \delta - i\beta$; according to the Snell−Descartes law of refraction, total external reflection occurs for grazing angles of incidence θ_{in} smaller than a critical angle $\theta_c = \sqrt{2\delta}$. This can be used to enhance surface sensitivity, as below this critical angle, an evanescent wave propagates at the surface with a penetration depth of only a few nanometers. Of course, the Born approximation breaks down under total reflection conditions, but a good approximation consisting in approximately describing the electromagnetic field at the surface by taking only refraction at the air−water interface into account can be applied.[20] Within this approximation, by performing the summation in eq 1 and explicitly writing the proportionality factors, we have for the differential scattering cross-section (power scattered per unit solid angle per unit incident flux):[20]

$$\frac{d\sigma}{d\Omega} = r_e |\, t(\theta_{in})|^2 |t(\theta_{sc})|^2 (\hat{\mathbf{e}}_{in}\cdot\hat{\mathbf{e}}_{sc})^2 |F(\boldsymbol{q})|^2 \times \frac{\sin^2(N_1\mathbf{q}\cdot\mathbf{a}/2)}{\sin^2(\mathbf{q}\cdot\mathbf{a}/2)} \frac{\sin^2(N_2\mathbf{q}\cdot\mathbf{b}/2)}{\sin^2(\mathbf{q}\cdot\mathbf{b}/2)} \quad (2)$$

where N_1 and N_2 are limited to the illuminated area. $r_e = 2.815 \times 10^{-15}$ m is the Thomson electron radius. $t(\theta_{in})$ and $t(\theta_{sc})$ are the Fresnel transmission coefficients between air and water for the grazing angle of incidence θ_{in} and the grazing angle of diffraction θ_{sc}, respectively. The coefficient $t(\theta_{in})$ represents a good approximation to the actual surface field, while $t(\theta_{sc})$ describes how the diffracted wave propagates to the detector.[20] These coefficients are responsible for the so-called Vineyard peaks at θ_c in the "Bragg rods" (vertical dependence of the diffracted intensity).[21] $(\hat{\mathbf{e}}_{in}\cdot\hat{\mathbf{e}}_{sc})^2$ is the polarization factor: $\hat{\mathbf{e}}_{in}$ is the polarization vector of the incident field, and $\hat{\mathbf{e}}_{sc}$ that of the scattered field. Equation 2 has to be integrated over the detector solid angle to obtain the intensity measured in an experiment. If the diffraction peak is not resolution limited, this simply amounts to a multiplication with the detector solid angle $\Delta\Omega$.

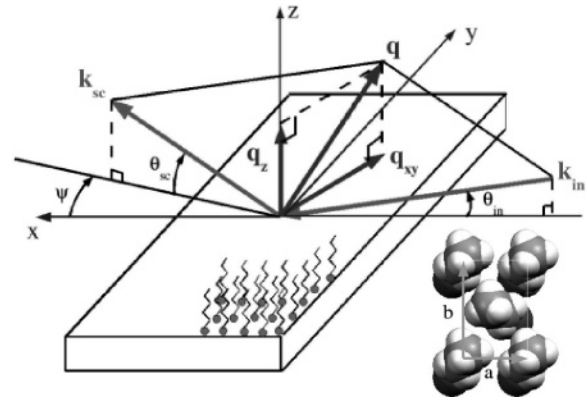

Figure 1. Geometry of the experiment. The incident wave-vector $\mathbf{k}_{in}$ makes a grazing angle of incidence θ_{in} with the water surface, whereas the scattering direction is defined by the angle $\mathbf{k}_{ac}$. The in-plane component of the wave-vector transfer $\mathbf{q} = \mathbf{k}_{sc} - \mathbf{k}_{in}$ is $\mathbf{q}_{||}$ and its vertical component is q_z. Inset: rectangular centered unit cell used for indexation.

For sufficiently large crystallites, eq 2 reduces to

$$\frac{d\sigma}{d\Omega} = 4\pi^2 r_e |t(\theta_{in})|^2 |t(\theta_{sc})|^2 (\hat{\mathbf{e}}_{in}\cdot\hat{\mathbf{e}}_{sc})^2 \times \frac{A}{|\mathbf{a}\times\mathbf{b}|^2} \sum_{h,k} |F(h,k,q_z)|^2 \delta(\mathbf{q}_{||} - \mathbf{G}) \quad (3)$$

where A is the illuminated area, $\mathbf{q}_{||}$ is the in-plane component of the wave-vector transfer, and $\mathbf{G} = 2\pi h\mathbf{a}^* + 2\pi k\mathbf{b}^*$ is a reciprocal lattice wave-vector. By introducing the atomic form factor f_j and writing the electron density as the sum of the contributions of the different atoms in the unit cell, $F(h, k, q_z) = \sum_j f_j \exp[2i\pi(hx_j + ky_j) + iq_z\zeta_j]$, with q_z the vertical component of the wave-vector transfer, h, k the Miller indices, and (x_j, y_j, z_j) the fractional coordinates of the jth atom in the unit cell located at height ζ_j.

3. Experimental Details

The experiments reported here were carried out at the Troïka II beamline of the European Synchrotron Radiation Facility (ESRF). The monochromatic incident 7.975 keV X-ray beam (wavelength $\lambda = 0.155$ nm) was first extracted from the polychromatic beam of the undulator source by using a two-crystal diamond (111) monochromator. Higher harmonics were eliminated by using two platinum-coated glass mirrors, also used to set the grazing angle of incidence θ_{in} on the liquid surface (Figure 1). The intensity of the incident beam was monitored by measuring the air scattering by using a NaI(Tl) scintillator. To limit background, θ_{in} was fixed to 1.83 mrad, which is below the critical angle for total external reflection $\theta_c = 2.69$ mrad; $\theta_{in} = 0.68\theta_c$, and the penetration of the evanescent wave was ≈5 nm. The incident beam size was 1 mm × 0.5 mm ($H \times V$), set by a 150 mm Soller collimator with 1.4 mrad (5.66×10^{-3} Å^{-1}) resolution in front of the vertically mounted position-sensitive detector (PSD). Experiments consisted in scanning the PSD around a vertical axis (angle ψ). The vertical dependence of X-ray scattering was recorded by using the PSD for q_z values from 0 to 0.5 Å^{-1}.

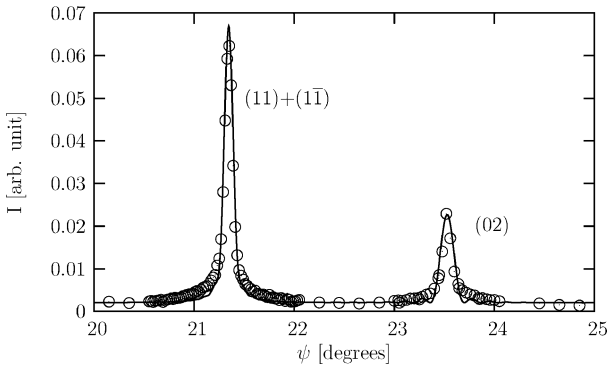

Figure 2. Grazing incidence diffraction from a behenic acid film in the S phase at $T = 16.1$ °C and $\Pi = 32.1$ mN/m (circles); $a = 0.5027$ nm and $b = 0.7265$ nm. Under these conditions $F(1,1) = F(0,2)$. The solid line is a fit using eq 2 as described in the text.

A Langmuir trough equipped with a movable single barrier for the compression of the film and a Wilhelmy balance for surface pressure measurement was mounted on an active antivibration system on the diffractometer. The trough was filled with ultrapure deionized water from a Milli-Q 185+ Millipore system. Fatty acids $C_{n-1}H_{2n-1}COOH$ were purchased from Fluka (>99% purity) and used as obtained. Different chain lengths were investigated: palmitic acid n=16 (C_{16}), stearic acid n=18 (C_{18}), arachidic acid n=20 (C_{20}), and behenic acid n=22 (C_{22}). The fatty acids were first dissolved in chloroform (Merck, analytical grade) to a concentration of ≈1 g/L, and approximately 100 μL of the solution was carefully spread on the water surface. The film was then compressed to a given surface pressure, measured by using a Wilhelmy plate. The pressure was not kept constant during X-ray measurements. The temperature was regulated by using the water of a thermal bath.

Four phases were investigated: The L_2 phase (rectangular centered unit cell with molecules tilted toward their nearest neighbors), L_2' phase (rectangular centered unit cell with molecules tilted toward their next-nearest neighbors), S phase (rectangular centered unit cell with untilted molecules), and the rotator hexagonal LS phase. See, for example, ref 10 for a review of earlier structural studies of the different phases.

Only first-order peaks were measured in this study. We used a peak indexation related to a rectangular two-molecule cell (with a small cell parameter a and a large cell parameter b). The (11)(1$\bar{1}$) and (02) peaks are degenerate in the hexagonal LS phase, as well as the (11) and (1$\bar{1}$) peaks in the S, L_2, and L_2' phases for which two peaks are measured.

4. Data Extraction and Processing

Eqs 2 and 3 contain all the terms necessary to calculate a diffraction curve. This has been done in Figure 2 for behenic acid in the S phase at $T = 16.1$ °C and $\Pi = 32.1$ mN/m. Under these conditions, $F(1, 1) = F(0, 2)$, which simplifies the calculations. A very good agreement was obtained with $N_1 = 180$ and $N_2 = 80$, in agreement with the well-known fact that the crystallinity in the S phase is much better along **a** than along **b**. These numbers are also in good agreement with a direct application of Scherrer's formula relating the coherence length L of a reflection to its full width at half-maximum Δq as $L \approx 0.9 \times 2\pi/\Delta q$,[22] which would lead to $N_1 = 140$ and $N_2 = 80$.

Whereas this approach could be pursued, it is in fact much more advantageous to take advantage of all the background of three-dimensional X-ray crystallography. Following ref 23, we therefore decided to use the SHELX-97 program to analyze our data.

As this program was initially designed for a three-dimensional crystal structure refinement, data processing is necessary to use it for a two-dimensional powder, oriented with respect to the water surface but randomly oriented around the normal to the surface. In particular, this implies transforming our data into a set of structure factors $F^2(h, k, l)$. First, following ref 23, we assign l Miller indices according to a virtual c axis (≃650 Å) so as to match the sampling along the PSD.

We then calculate $F^2(h, k, l)$ from our data. We proceed by calculating the integrated (h, k) intensity for each l (or q_z) value. This integration is similar to the calculation leading from eq 2 to eq 3 and gives a set of $F^2(h, k, l)$ multiplied by several factors. Two different methods were used to perform the integration: When we had a well-defined flat baseline and well-separated peaks (as in LS or S phases), we performed a direct numerical integration over q_{xy} after background subtraction. When this was not possible, in particular because of overlapping peaks such as in L_2 or L_2' phases, the peaks were fitted by using a Lorentzian or pseudo-Voigt function from which the (h, k) integrated intensity was calculated. Both methods yielded similar results when applicable. Errors bars were calculted assuming Poisson statistics and a negligible error on the intensity of the incident beam.

To finally obtain the set of $F^2(h, k, l)$ up to a common multiplicative factor, the data have to be corrected for those proportionality factors that depend on the scattering angle.

First, the diffracted intensity depends on the illuminated area. This dependence is explicit in eq 3 and follows from the fact that $I \propto N_1N_2$ in eq 2 as the height of the peaks scales as $(N_1N_2)^2$, whereas their width scales as $1/(N_1N_2)$. As ψ is scanned, the area seen by the detector decreases as (L/sin ψ).[20]

Second, there is the polarization factor, $(\hat{\mathbf{e}}_{in}\cdot\hat{\mathbf{e}}_{sc})^2 = \cos^2\psi$ (eqs 2 and 3).

Finally, our films are not single crystals and the (h, k) integrated intensity results from contributions of many crystallites in reflection position. Considering an homogeneous distribution of crystallite orientations between ϕ and $\phi + \delta\phi$, the crystallites fulfilling the diffraction condition lie in Fourier space on an infinitesimal arc of length $q_{\parallel}\delta\phi = 2k_0 \sin(\psi/2)\delta\phi$ perpendicular to $\mathbf{q}_{\parallel}$, whereas the finite resolution amounts to scanning an arc $k_0\delta\psi$ perpendicular to $\boldsymbol{k}_{sc}$. As the angle between $\boldsymbol{k}_{sc}$ and $\mathbf{q}_{\parallel}$ is $\psi/2$, the infinitesimal area in Fourier space corresponding to $\delta\phi$ and $\delta\psi$ is $\delta q_x\delta q_y = 2k_0^2 \sin(\psi/2) \cos(\psi/2)\delta\phi\delta\psi = k_0^2 \sin\psi\delta\phi\delta\psi$. Therefore, the angular integration leads to a result that is larger than the result of the integration in Fourier space leading to $|F(h, k, q_z)|^2$ (see eq 3) by a factor (1/sin ψ), the so-called Lorentz factor.

We therefore need to multiply the integrated intensities (1/$\tan^2\psi$) to finally obtain $F^2(h, k, l)$.

Because of the limited number of diffraction data, a structure refinement using SHELX-97 is difficult without applying numerous constraints or restraints. We rather chose to use the known chemical structure of fatty acid molecules by imposing atomic coordinates in a molecular model (Figure 3a) that allowed us to fit relevant parameters such as hydrocarbon backbone plane azimuth, headgroup rotation, or gauche defects in the hydrocarbon chain. Accordingly, we only use SHELX-97 to calculate the theoretical reflection data set based on the model, which is compared with the experimental reflection data set. Averaging over all equivalent reflections is performed before calculating χ^2; for example, we average $F^2(1, 1, l)$, $F^2(-1, -1, l)$, $F^2(1, -1, l)$, $F^2(-1, 1, l)$ for the S phase. Note that the superposition of the $F^2(h, k, l)$ and $F^2(-h, -k, l)$ can be automatically taken into account by SHELX by imposing a

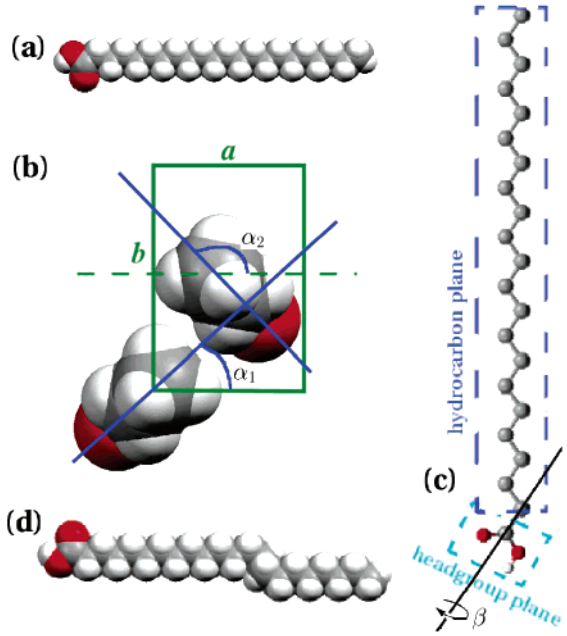

Figure 3. (a) Molecular model of a behenic acid molecule ($C_{21}H_{41}$-COOH). Spheres represent the atomic van der Waals radii. (b) Top view of the unit cell showing the azimuths α_1 and α_2 of the backbone planes of the two molecules. (c) Headgroup plane rotation relative to the backbone plane. (d) Gauche defect. All figures were drawn using the mercury software.[24]

twinning of the crystal about the (**a**, **b**) plane as $F^2(-h, -k, l) = F^2(h, k, -l)$ according to Friedel's law.[23]

SHELX-97 calculates the model reflection data set by using the kinematic theory of diffraction. Atoms are treated as spheres of van der Waals radius to which independent Debye−Waller coefficients can be applied. Moreover, SHELX-97 can calculate the hydrogen atomic coordinates for a sp_3 and sp_2 carbon, which simplify the model creation and the fitting speed.

5. Results

5.1. Fitting of molecular parameters. *5.1.1. Backbone Plane Azimuth.* The azimuths α_1 and α_2 of the backbone planes of the two molecules in the unit cell are represented on Figure 3b.

As a fatty acid molecule has no internal symmetry axis, we have in principle to consider all values of α from 0 to 360°. However, for our powder, we can limit the fit to the interval [0°, 180°] for the first molecule, and to [α_1, α_1 + 180°] for the second one. This domain is indicated by white solid lines in Figure 8.

As can be seen on Figure 4, the relative intensity of the (11)-($1\bar{1}$) and (02) peaks is very sensitive to the azimuth of the backbone planes. Changing the azimuth modifies the interferences between the waves scattered by the atoms belonging to the two molecules, but the vertical dependence of the scattered intensity remains unchanged. Therefore, upon azimuth rotation, the shape of the curves is not modified, but their relative intensity is.

5.1.2. Headgroup Plane Rotation. The carboxylic acid headgroup −COOH of fatty acids has a planar geometry. The angle β between the chain backbone plane and the carboxylic acid plane is defined in Figure 3c. The origin $\beta = 0°$ has been chosen with the C_3−C_2 and C_1=O bonds on the same side of the C_2−C_1 bond, where the carboxyl and carbon chain groups are coplanar. This cis position has been assumed in keeping with known three-dimensional crystal structures.[25]

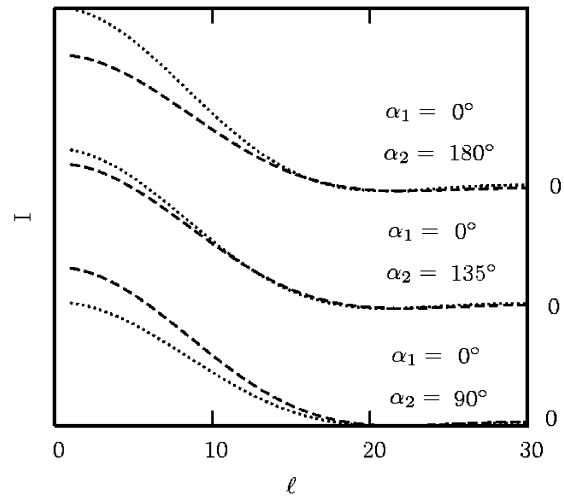

Figure 4. Effect of backbone plane azimuth rotation for behenic acid (C_{22}) in the S phase. The dashed line represents the (11)($1\bar{1}$) reflection, and the dotted line represents the (02) reflection.

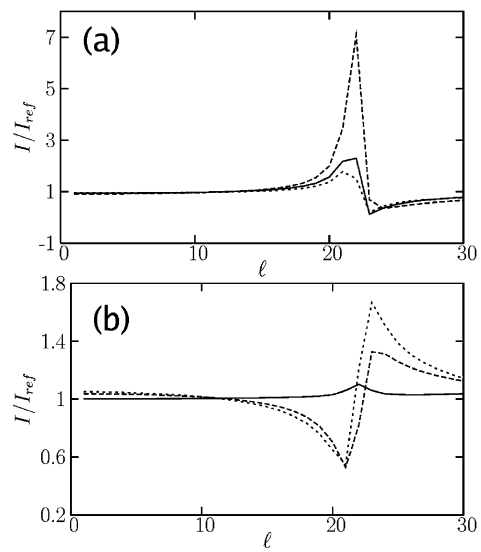

Figure 5. Effect of the headgroup plane rotation β for behenic acid (C_{22}) in the S phase with α_1 = 45° and α_2 = 135°. To make the differences more visible, the intensity for different β values are represented relative to the intensity for $\beta_1 = \beta_2 = 0°$; (a) (02) reflection, (b) (11)($1\bar{1}$) reflection; solid line: $\beta_1 = 0°$ and $\beta_2 = 45°$; dashed line: $\beta_1 = 0°$ and $\beta_2 = 90°$; dotted line: $\beta_1 = 0°$ and $\beta_2 = 135°$.

As the headgroup rotation changes the internal geometry of the molecule, this parameter modifies the shape of the (11)($1\bar{1}$) and (02) curves, contrary to the azimuth of the chain backbone. We can see in Figure 5 that changes are especially located at l values around 20 due to the thickness of the headgroups compared to the chains. This effect is limited compared to the azimuth rotation, but the change in the profile makes the measurement sensitive to it.

5.1.3. Gauche Defects. The position of each carbon i is defined by a dihedral angle ψ_i (rotation angle around the C_{i-1}−C_i axis). This angle can take three different values: $\psi_i = 0°$ for a trans link called t, $\psi_i = 120°$ for a gauche link called g^+, and $\psi_i = 240°$ for a gauche link called g^-. A gauche defect is characterized by the sequence $g^+ - t - g^-$ or $g^- - t - g^+$ (Figure 3d).

To simulate chain disorder, we have put one gauche defect at an arbitrary position of one chain in a supercell of eight chains. The result of this calculation is represented in Figure 6.

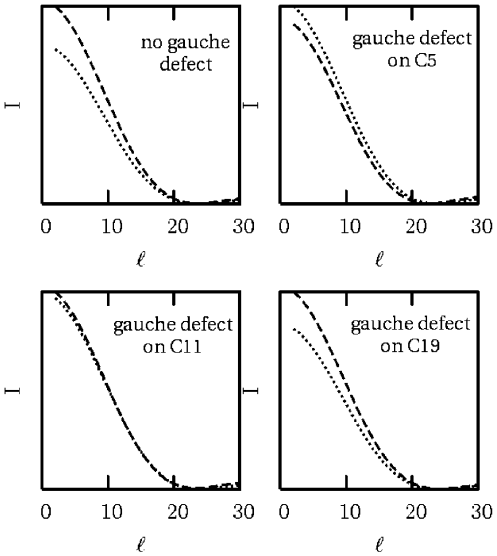

Figure 6. Effect of a gauche defect at different positions on one molecule in a supercell of 8 molecules for arachidic acid (C_{20}) in the S phase ($\alpha_1 = 120°$, $\alpha_2 = 210°$). The dashed line represents the (11)-($\bar{1}$1) reflection, and the dotted line represents the (02) reflection.

Again, as the chain geometry is changed, the Bragg-rod profiles are markedly modified.

We also made possible the rotation of the terminal methyl group, but our measurement was revealed to be insensitive to this very small change in the molecule conformation.

5.1.4. Vertical Debye−Waller Factor. We took account of the vertical Debye−Waller factor U_z with the classical exponential decay:

$$I_{U_z} = I \times e^{-2\pi^2 l^2 U_z/c^2} \tag{4}$$

As expected, the effect is stronger for large l values.

5.2. LS Phase. The LS phase is a high-pressure phase where all molecules are untilted and free to rotate. They are arranged in a hexagonal cell, which implies that there is only one degenerate peak for the (11)($\bar{1}$1) and (02) reflections. We modeled the free rotation by allowing the hydrocarbon plane azimuth to take all values in the range [0−360°] with a step of 18° and an equal probability for each position.

The data of Figure 7 were obtained by fitting the experimental reflection data set of a palmitic acid (C_{16}) film at $\Pi = 28.5$ mN/m and $T = 1$ °C.

As the molecules are free to rotate, the only interesting fitting parameters are a gauche defect position and the Debye−Waller factors.

χ^2 increases with increasing U_{xy} and decreases with increasing U_z. The best χ^2 is obtained for $U_z = 11.4$ Å^2 and $U_{xy} = 0.1$ Å^2. The inset of Figure 10 presents the effect of a gauche defect on one chain in a supercell of eight molecules. χ^2 is large except when the defect is located close to the top of the chain.

5.3. S Phase. The S phase is a high-pressure phase where all molecules are untilted and are arranged in a distorted hexagonal cell. There are two lowest-order peaks corresponding to the (02) reflection and the degenerate (11) and ($\bar{1}$1) reflections. Herringbone ordering is expected in this phase ($\alpha_2 - \alpha_1 \approx 90°$).[15,26]

We first consider the hydrocarbon chain backbone azimuth α. Figure 8a presents results of a fit for an arachidic acid film (C_{20}) at $T = 4.9$ °C. The best χ^2 values are obtained for $\alpha_2 - \alpha_1 = 90°$. It is remarkable that whatever the α_1 and α_2 values are, the χ^2 minima are concentrated in the $\alpha_2 - \alpha_1 = 90°$ valley, showing that herringbone ordering is a very robust result of

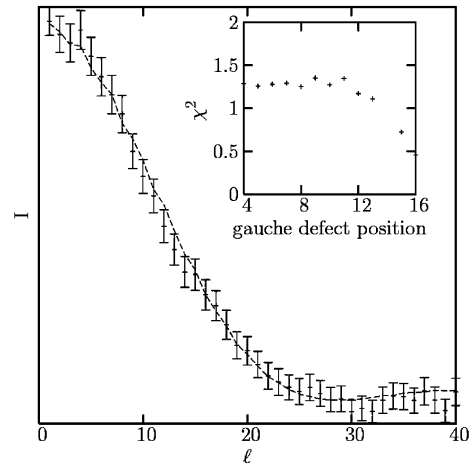

Figure 7. Experimental Bragg rod profile (points) and fit (dotted line) for a LS phase of palmitic acid (C_{16}) at $\Pi = 28.5$ mN/m and $T = 1$ °C. The best χ^2 value (0.42) was obtained with no gauche defect, $U_{xy} = 0.1$ Å^2, and $U_z = 11.4$ Å^2 all along the molecule. Inset: represents the effect of a gauche defect position on χ^2 for one molecule in a supercell of eight molecules.

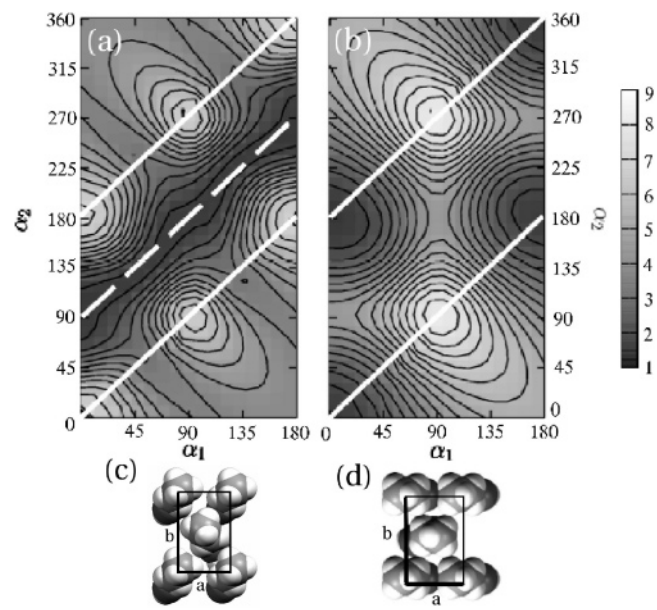

Figure 8. Fit results for arachidic acid (C_{20}) at $T = 4.9$ °C and $\Pi = 27.3$ mN/m (a) and $\Pi = 37.4$ mN/m (b); χ^2 (grey scale on the right) in the (α_1, α_2) plane. Solid white lines enclose nonequivalent configurations. The fitting parameters were α_1, α_2, and the headgroup rotation angle for each molecule. The white dashed line in (a) corresponds to herringbone ordering $\Delta\alpha = 90°$ (c). Best fits in b yield $\Delta\alpha = 180°$ (d).

the fit. To our knowledge, this is the first time that herringbone packing is directly determined without any ambiguity in the S phase. Crystal symmetry imposes a glide along the axis for this packing, but we obtained this result ab initio without this constraint. Parallel to this, the configurations $\alpha_1 = 90°$ with $\alpha_2 - \alpha_1 = 0°$ or 180° yield the highest χ^2 values.

Figure 8b presents the results of the fit for the same arachidic acid film, apparently in the S phase at a pressure of $\Pi = 37.4$ mN/m. The lowest χ^2 values now concentrate around ($\alpha_1 = 0°$, $\alpha_2 = 0°$), ($\alpha_1 = 0°$, $\alpha_2 = 180°$), ($\alpha_1 = 180°$, $\alpha_2 = 180°$), and ($\alpha_1 = 180°$, $\alpha_2 = 360°$), i.e., with hydrocarbon backbone planes parallel to the (ac) plane. As in the previous case, configurations $\alpha_1 = 90°$ with $\alpha_2 - \alpha_1 = 0°$ or 180° have the highest χ^2 values.

The α values corresponding to the best fits are plotted in Figure 9 as a function of surface pressure for arachidic acid

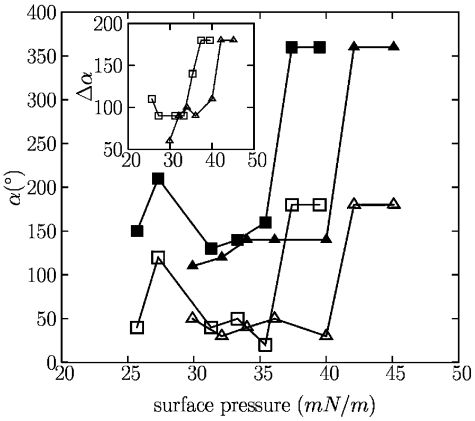

Figure 9. Azimuth values α_1 (empty symbols) and α_2 (full symbols) corresponding to best fits as a function of surface pressure for arachidic acid (C_{20}) at $T = 4.9$ °C (squares) and behenic acid (C_{22}) at $T = 16.1$ °C (triangles). $\Delta\alpha = \alpha_2 - \alpha_1$ is plotted as a function of surface pressure in the inset.

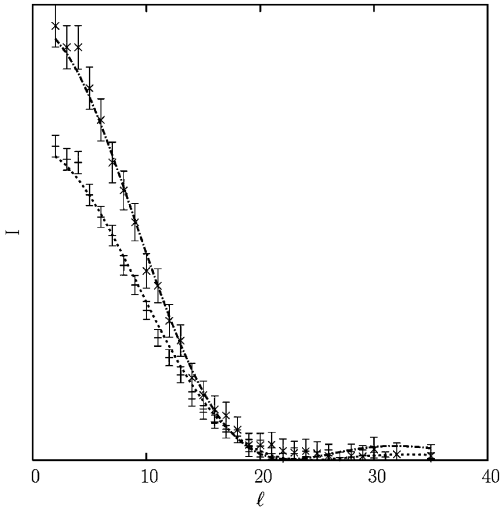

Figure 10. Experimental Bragg rod profile (points) and fit (dotted line) for a high-pressure phase of arachidic acid (C_{20}) at $\Pi = 37.4$ mN/m and $T = 4.9$ °C. The upper curve is the (02) data set, and the lower curve the (11) data set. The best χ^2 value (1.71) was obtained with no gauche defect, $U_{xy} = 0.1$ Å^2 and $U_z = 19.6$ Å^2 all along the molecule.

(C_{20}) and behenic acid (C_{22}). Better χ^2 are generally obtained for $p1g1$ symmetry ($\alpha_1 \approx 45°$, $\alpha_2 \approx 135°$) than for $p11g$ ($\alpha_1 \approx 135°$; $\alpha_2 \approx 225°$). There is an abrupt increase of α_1, α_2, and the azimuth difference $\Delta\alpha$ around $\Pi = 35$ mN/m for arachidic acid and $\Pi = 40$ mN/m for behenic acid, respectively. More precisely, for arachidic acid, α_1 increases from $37.5° \pm 11°$ to 180°, and α_2 increases from $145° \pm 11°$ to 360°. For behenic acid, α_1 increases from $40.0° \pm 9°$ to 180°, and α_2 increases from $130° \pm 13°$ to 360°. The azimuth difference $\Delta\alpha$, therefore, increases from 70° to 110° (herringbone packing) at lower pressures in the S phase to 0° or 180° (molecules in the *ac* plane) for very high surface pressures. Our results unambiguously show a transition from a phase with $p1g1$ symmetry (the S phase) to another phase with symmetry $p2gm$ at higher pressure.

Headgroup plane rotation was fitted together with the chain azimuths. Figure 11 presents the results for a film under the same conditions as in Figure 8. Our fits unambiguously show that the headgroup and hydrocarbon planes are coplanar. This could be expected from three-dimensional crystallography on

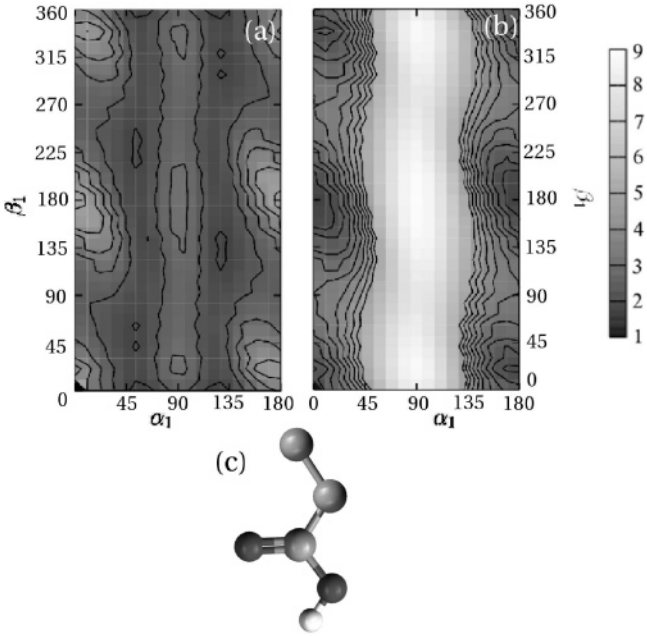

Figure 11. Fit results for arachidic acid (C_{20}) at $T = 4.9$ °C and $\Pi = 27.3$ mN/m (a) and $\Pi = 37.4$ mN/m (b); χ^2 (grey scale on the right) in the (α_1, β_1) plane. The fitting parameters were α_1, α_2, and the headgroup rotation angle for each molecule. Figure (c) represents the coplanar cis configuration with the lowest χ^2 value.

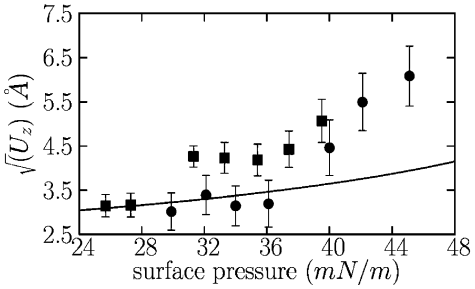

Figure 12. Vertical Debye−Waller factor $\sqrt{U_z}$ as a function of surface pressure in the S phase of arachidic acid (squares) at $T = 4.9$ °C and of behenic acid (circles) at $T = 16.1$ °C. The solid line represents the effect of capillary waves (as described in eq 5).

similar molecules,[27] but was never directly demonstrated on Langmuir films.

As in the LS phase, the vertical Debye−Waller factor U_z takes rather high values ($U_z = 14.1$ Å^2), while the horizontal Debye−Waller factor U_{xy} remains low ($U_{xy} = 0.1$ Å^2). Upon compression, the $\sqrt{U_z}$ value increases from ≈3.0 Å to ≈6.0 Å at the very high pressures where $\Delta\alpha$ is near 180° (Figure 12). Introduction of a gauche defect for one molecule in a supercell of eight molecules is always unfavorable whatever its position in the chain, but higher χ^2 values are obtained when defects are located closer to the headgroup.

6. Discussion

6.1. A New Phase for Very High Pressures. A glide plane along *a* ($p11g$ symmetry) or along *b* ($p1g1$ symmetry) is expected in the S phase as the (10) and (01) reflections have never been observed. Our measurements favor the $p1g1$ symmetry, with $\alpha_1 = 45°$ and $\alpha_2 = 135°$. This organization of the hydrocarbon chain planes was confirmed by our crystallographic analysis for pressures below 35 mN/m for arachidic acid and 40 mN/m for behenic acid. At higher pressures, we unambiguously demonstrate the existence of a new phase. In this new

phase, the molecules have their hydrocarbon planes parallel to the (*ac*) plane (α_1 and $\alpha_2 = 0°$ or 180°). Surprisingly, although a phase with *c*11*m* symmetry ($\Delta\alpha = 0°$) seems to be preferable to a phase with *p*2*gm* symmetry ($\Delta\alpha = 180°$) because 2-fold crystal symmetry is generally a disadvantage, we obtained better χ^2 for the *p*2*gm* symmetry.

It is interesting to note that this phase with *p*2*gm* cell symmetry, which has never been observed, corresponds to an energy minimum in lattice energy calculations.[15] The difference in transition pressure ≈5−10 mN/m between arachidic and behenic acid corresponds to what could be expected from the two additional methylene groups in behenic acid.

6.2. U_z Value in S Phase. The high U_z values, which we obtain in the S phase, are rather unexpected. A reasonable explanation is that this high U_z is partly due to thermally excited capillary waves: $U_z = U_z^{CW} + U_z^{S}$, where U_z^{CW} is the capillary wave contribution and U_z^{S} a static disorder. The capillary wave contribution can be estimated as follows:

$$U_z^{CW} = \frac{k_B T}{2\pi\gamma} \times \ln\frac{q_{min}}{q_{max}} \tag{5}$$

with γ the surface tension, q_{min} the lowest capillary excitation wave-vector in a single crystal (corresponding to domain size), and q_{max} the largest wave-vector (corresponding to the distance between molecules).[20] By using eq 5 with $\gamma = 30$ mN/m and $q_{min}/q_{max} \approx 1{:}100$ from a fit of peaks to eq 2, we obtain $\sqrt{U_z} \approx 3.0$ Å, which has the right order of magnitude and is represented as a solid line on Figure 12. It can be seen on Figure 12 that U_z is significantly larger than the capillary wave prediction at high pressure, above ≈35 mN/m. The difference can be seen as a larger roughness, as in Figure 12, or as a shift δ_z of one of the molecules in the unit cell with respect to the other one. Good fits could be obtained either with a larger U_z value or with δ_z values smaller than 0.2 nm, even for the highest pressure.

7. Concluding Remarks

Our ab initio approach allowed us to directly obtain near-atomic structural information as hydrocarbon backbone plane azimuth and headgroup orientation in fatty acid Langmuir films. We confirmed the herringbone packing generally inferred from the comparison with three-dimensional structures. In addition, this method allowed us to evidence a new high-pressure phase with symmetry *p*2*gm*, which has never been observed but corresponds to a minimum in the lattice energy. This method opens the way to submolecular structural studies of more complex two-dimensional systems. In a first step, this should enable one to precisely determine the role of hydrogen bonds in the tilted phases of fatty acids, alcohols, or esters.

Acknowledgment. The use of the SHELX-97 software by George Sheldrick is gratefully acknowledged. We greatly benefited from discussion with Sophie Cantin-Rivière, Thierry Prangé, and Pierre Thuéry.

References and Notes

(1) Bibo, A. M.; Knobler, C. M.; Peterson, I. R. *J. Phys. Chem.* **1991**, *95*, 5591−5599.
(2) Kjaer, K.; Als-Nielsen, J.; Helm, C. A.; Laxhuber, L. A.; Möhwald, H. *Phys. Rev. Lett.* **1987**, *58*, 2224−2228.
(3) Dutta, P.; Peng, J. B.; Lin, B.; Ketterson, J. B.; Prakash, M.; Georgopoulos, P.; Ehrlich, S. *Phys. Rev. Lett.* **1987**, *58*, 2228−2231.
(4) Grayer Wolf, S.; Leiserowitz, L.; Lahav, M.; Deutsch, M.; Kjaer, K.; Als-Nielsen, J. *Nature* **1987**, *328*, 63−66.
(5) Lin, B.; Shih, M. C.; Bohanon, T. M.; Ice, G. E.; Dutta, P. *Phys. Rev. Lett.* **1990**, *65*, 191−194.
(6) Kenn, R. M.; Böhm, C.; Bibo, A. M.; Peterson, I. R.; Möhwald, H.; Als-Nielsen, J.; Kjaer, K. *J. Phys. Chem.* **1991**, *95*, 2092−2097.
(7) Bommarito, G. M.; Foster, W. J.; Pershan, P. S. *J. Chem. Phys.* **1996**, *105*, 5265−5284.
(8) Als-Nielsen, J.; Möwald, H. In *Handbook of Synchrotron Radiation*; Ebashi, S., Koch, M., Rubinstein, E., Eds.; Elsevier Science: Amsterdam, 1991; Vol. 4, pp 1−53.
(9) Als-Nielsen, J.; Jacquemain, D.; Kjaer, K.; Leveiller, F.; Lahav, M.; Leiserowitz, L. *Phys. Rep.* **1994**, *246*, 251−313.
(10) Kaganer, V. M.; Möhwald, H.; Dutta, P. *Rev. Mod. Phys.* 1999, *71*, 779−819.
(11) Solomonov, I.; Weygand, M. J.; Kjaer, K.; Rapaport, H.; Leiserowitz, L. *Biophys. J.* **2005**, *88*, 1809−1817.
(12) Rapaport, H.; Kjaer, K.; Jensen, T. R.; Leiserowitz, L.; Tirrell, D. A. *J. Am. Chem. Soc.* **2000**, *122*, 12523−12529.
(13) Kitaigorodskii, A. I. *Organic Chemical Crystallography*; Consultant Bureau: New York, 1961.
(14) Durbin, M. K.; Richter, A. G.; Yu, C.-J.; Kmetko, J.; Bai, J. M.; Dutta, P. *Phys. Rev. E* **1998**, *58*, 7686−7690.
(15) Kuzmenko, I.; Kaganer, V. M.; Leiserowitz, L. *Langmuir* **1998**, *14*, 3882−3888.
(16) Leveiller, F.; Jacquemain, D.; Leiserowitz, L.; Kjaerand, K.; Als-Nielsen, J. *J. Phys. Chem.* **1992**, *96*, 10380−10389.
(17) Jacquemain, D.; Leveiller, F.; Weinbach, S. P.; Lahav, M.; Leiserowitz, L.; Kjaer, K.; Als-Nielsen, J. *J. Am. Chem. Soc.* **1991**, *113*, 7684−7691.
(18) Wang, J.-L.; Leveiller, F.; Jacquemain, D.; Kjaer, K.; Als-Nielsen, J.; Lahav, L.; Leiserowitz, L. *J. Am. Chem. Soc.* **1994**, *116*, 1192−1204.
(19) Jacquemain, D.; Grayer Wolf, S.; Leveiller, F.; Frolow, F.; Eisenstein, M.; Lahav, M.; Leiserowitz, L. *J. Am. Chem. Soc.* **1992**, *114*, 9983−9989.
(20) Daillant, J.; Alba, M. *Rep. Prog. Phys.* **2000**, *63*, 1725−1777.
(21) Vineyard, G. H. *Phys. Rev. B* **1982**, *26*, 4146−4159.
(22) Guinier, A. *X-ray Crystallographic Technology*; Hilger and Watts: London, 1952; Chapter 10, pp 235−237.
(23) Rapaport, H.; Kuzmenko, I.; Lafont, S.; Kjaer, K.; Howes, P.; Als-Nielsen, J.; Lahav, M.; Leiserowitz, L. *Biophys. J.* **2001**, *81*, 2729−2736.
(24) Bruno, I. J.; Cole, J. C.; Edgington, P. R.; Kessler, M. K.; Macrae, C. F.; McCabe, P.; Pearson, J.; Taylor, R. *Acta Crystallogr. B* **2002**, *58*, 389−397.
(25) Leiserowitz, L.; Schmidt, G. M. J. *Acta Crystallogr.* **1965**, *18*, 1058.
(26) Fradin, C.; Daillant, J.; Braslau, A.; Luzet, D.; Alba, M.; Goldmann, M. *Eur. Phys. J. B* **1998**, *1*, 57−69.
(27) Leiserowitz, L. *Acta Crystallogr. B* **1976**, *32*, *775*.